International Journal of Pharmaceutics 636 (2023) 122647

Contents lists available at ScienceDirect

International Journal of Pharmaceutics

journal homepage: www.elsevier.com/locate/ijpharm

Biphasic burst and sustained transdermal delivery in vivo using an AI-optimized 3D-printed MN patch

Arvind Bagde [a], Satyanarayan Dev [b,**], Lalitha Madhavi K. Sriram [c], Shawn D. Spencer [d], Anilkumar Kalvala [a], Aakash Nathani [a], Oluwaseyi Salau [a], Keb Mosley-Kellum [a], Harshil Dalvaigari [e], Swaminathan Rajaraman [f], Avra Kundu [f], Mandip Singh [a,*]

[a] College of Pharmacy and Pharmaceutical Sciences, Florida A&M University, Tallahassee, FL, USA
[b] College of Agriculture and Food Sciences, Florida A&M University, Tallahassee, FL 32307, USA
[c] Florida State University, Tallahassee, FL 32307, USA
[d] Philadelphia College of Osteopathic Medicine, Philadelphia, PA 19131, USA
[e] James S. Rickards High School, Tallahassee, FL 32301, USA
[f] University of Central Florida, Orlando, FL 32816, USA

ARTICLE INFO

Keywords:
Dissolving microneedles
3D printing
Photoinitiator
LAP
Artificial intelligence
Quality by design

ABSTRACT

The objective of the present study was to fabricate microneedles for delivering lipophilic active ingredients (APIs) using digital light processing (DLP) printing technology and quality by design (QbD) supplemented by artificial intelligence (AI) algorithms. In the present study, dissolvable microneedle (MN) patches using ibuprofen (IBU) as a model drug were successfully fabricated with DLP printing technology at ~ 750 μm height, ~250 μm base diameter, and tip with radius of curvature (RoC) of ~ 15 μm. MN patches were comprised of IBU, photoinitiator, Lithium phenyl (2,4,6-trimethylbenzoyl) phosphinate (LAP), polyethylene glycol dimethacrylate (PEGDAMA)550 and distilled water and were developed using the QbD optimization approach. Optimization of print fidelity and needle morphology were achieved using AI implementing a semi-supervised machine learning approach. Mechanical strength tests demonstrated that IBU MNs formed pores both on Parafilm M® and human cadaver skin. IBU-MNs consisting of 0.23 %w/v and 0.49 %w/v LAP with 10 %w/v water showed ~ 2 mg/cm^2 sustained drug permeation at 72 h in skin permeation experiments with flux of ~ 40 μg/cm^2/h. Pharmacokinetic studies in rats displayed biphasic rapid first-order absorption with sustained zero-order input of Ko = 150ug/hr, $AUC_{0\text{-}48h}$ = 62812.02 ± 11128.39 ng/ml*h, Tmax = 2.66 ± 1.12 h, and Cmax = 3717.43 ± 782.25 ng/ml (using 0.23 %w/v LAP IBU MN patch). An in vitro in vivo relation (IVIVR) was conducted identifying a polynomial relationship between patch release and fraction absorbed in vivo. This study demonstrates fabrication of dissolvable DLP-printed microneedle patches for lipophilic API delivery with biphasic rapid first-order and sustained zero-order release.

1. Introduction

MN arrays have been used to encapsulate a variety of pharmaceutical drugs, proteins, and peptides for transdermal delivery through the stratum corneum layer of the skin (Affram et al., 2017; Aksu et al., 2012). The desirability of this administration method may be preferable over traditional intravenous needles due to minimal invasiveness, reduced pain, ease-of-use and wide range of tailorable release patterns into the dermis. Moreover, unlike other transdermal drug delivery systems including nanoparticles and permeation enhancers, MNs directly pierce into the skin and overcome the stratum corneum barrier to deliver the API transdermally (Griffin et al., 1993; Kulkarni et al., 1997; Singh et al., 1999; Shaik et al., 2001; Shaik et al., 2004; Patel et al., 2009; Patel et al., 2014; Patel et al., 2016a, 2016b; Affram et al., 2017; Chowdhury et al., 2017; Godugu et al., 2017; Fu et al., 2021). Recently, 3D printing technology for MN development has garnered attention as a viable method of production because of numerous advantages over micro-molding techniques such as increased efficiency and high

* Corresponding author.
** Co-corresponding author.
E-mail addresses: satyanarayan.dev@famu.edu (S. Dev), mandip.sachdeva@famu.edu (M. Singh).

https://doi.org/10.1016/j.ijpharm.2023.122647
Received 9 November 2022; Received in revised form 17 January 2023; Accepted 22 January 2023
Available online 6 February 2023

throughput processing, reproducibility, and single step production (Yang et al., 2021). 3D printing has not only been used for transdermal delivery of small APIs, but also to deliver large molecules including insulin. Pere et al and Economidou et al investigated transdermal delivery of insulin using 3D stereolithography (SLA) printed MNs which were coated with insulin formulation using inkjet printer (Pere et al., 2018, Economidou et al., 2019). Light-based photopolymerization 3D printing methods, such as Digital Light Processing (DLP) avoid the constraints of Fused Deposition Modeling (FDM) printing and are able to achieve superior print resolution through UV polymerization (Nukala et al., 2019). DLP allows for direct printing of MN containing the drug polymer solution, thus saving time and cost in manufacturing. Polymer properties and photoinitiator (PI) are important factors to be considered in material selection of dissolvable MN because the components must be non-toxic and have sufficient strength to puncture the skin following polymerization. Further, drug solubility in the pre-polymer solution allows for increased drug loading into the MN compared to simply coating the needles. Release characteristics of the drug can also be changed by varying the molecular weight of the polymer, photoinitiator concentration, water content, and pH. (Altuna et al., 2010, Stavrinidis et al., 2016). Lithium phenyl (2,4,6-trimethylbenzoyl) phosphinate is a free-radical photoinitiator which has demonstrated advantages over other photoinitiators, such as high water solubility and low cytotoxicity for biodegradable applications (Fairbanks et al., 2009). Nguyen et al reported that < 0.5 %w/w LAP concentration was cyto-compatible in cytotoxicity assays on human primary renal proximal tubule epithelial cells (hRPTECs) (Nguyen et al., 2019). Duchi et al studied the co-axial bioprinting of scaffold using LAP as a photoinitiator with high cell viability suggesting its cytocompatibility (Duchi et al., 2017). Further, Fairbanks et al demonstrated the potential application of LAP for photoencapsulation of mammalian cells with > 95 % cell viability for fibroblast encapsulated in PEG diacrylate and LAP combination hydrogel (Fairbanks et al., 2009).

There are limited reports on the fabrication and transdermal in vivo performance of dissolvable microneedles using high-resolution DLP printing technology. Uddin et al., Lu et al. and Xenakakis et al., reported on the use of SLA-based MN development where they evaluated delivery of small molecules into the skin for topical applications (Lu et al., 2015, Xenikakis et al., 2019, Uddin et al., 2020) Khosraviboroujeni et al. reported on a PLA-based FDM developed MN however did not describe its vivo release and absorption (Khosraviboroujeni et al., 2022) Yao et al. reported multifunctional hydrogel MNs manufacturing using high-precision digital light processing (H—P DLP) system with industrial free radical generator bisacylphosphane oxide (BAPO) as a photoinitiator, and overall MN performance was evaluated ex-vivo (Yao et al., 2019). Johnson et al. developed MNs using 2,4,6-trimethylbenzoyldiphenyl phosphine oxide (TPO) as photoinitiator with a continuous liquid interface production method, and also evaluated its MN performance ex vivo (Johnson et al., 2016). We previously reported on development of a TPO-based DLP printed intelligent MN array (iμNA) as a stimuli responsive device showing distinct release characteristics from external stimuli such as temperature and pH (Kundu et al., 2020). The performance and mechanism for sustained transdermal delivery of a small molecule from a high-resolution 3D-printed dissolvable MN resin formulation has not been published yet.

Here we advance our understanding of MN patch performance following a Quality-by-Design (QbD) approach, which utilizes numerous factors of evaluation and has been widely used in pharmaceutical industry for consistency and quality of the product (Dayal et al., 2005, Bagde et al., 2019a; Nukala et al., 2019a; Palekar et al., 2019). In addition, we employed a machine learning approach via Convolution Neural Networks to understand and analyze the MN patch image for optimal print fidelity and needle morphology. Convolution Neural Network architecture and algorithms demonstrate excellent performance with image data and is currently-one of the best performing methods of optimizing 3D-printing (Kandimalla et al., 1999, Sriram et al., 2018, Sriram et al., 2019). The objective of the present study was to develop resin formulation compatible for both SLA and DLP printing of dissolvable MNs patches using the QbD approach and to evaluate DLP printed MN patches for its release and performance. Optimization of print fidelity and needle morphology was achieved using a semi-supervised machine learning approach. The optimized MN patches were evaluated for mechanical strength studies, and evaluated for in vitro, ex vivo, and in vivo pharmacokinetics (PK) using ibuprofen as a model drug. Ibuprofen is a lipophilic short half-life small molecule and was studied due to its relatively high apparent permeability membrane coefficient and was evaluate mostly patch performance in lieu of permeation effects (Hoffmann et al., 2018).

2. Materials and Methods:

2.1. Materials:

PEGDAMA 550 and LAP were purchased from Sigma Aldrich, MO, USA. Micro DLP 3D printer was purchased from Kudo3D, CA, USA and 3 M Tegaderm™ waterproof transparent dressing from VWR, USA. Formlabs Form 2 SLA printer was purchased from Somerville, MA, USA.

2.2. Animals

Sprague Dawley (SD) rats were purchased from Charles River Laboratories, Wilmington, MA for in vivo PK studies. The animals were kept in cages with beddings and maintained under controlled conditions of 22 ± 2 °C, 12:12 hr light:dark cycle, and 50 ± 15 % relative humidity. The rats were provided with feeding (Teklad, Harlan, USA) and water ad libitum. They were housed at Florida A&M University in accordance with the Guide for the Care and Use of Laboratory Animals and Association for Assessment and Accreditation of Laboratory Animal Care (AAALAC) and were acclimatized to laboratory conditions for a week before the onset of all experiments (Care and Animals 1986, Council 2010). The Institutional Animal Care and Use Committee (IACUC) at Florida A& M University approved all animal protocols that were observed in this study.

2.3. SLA 3D printing of microneedle patches

2.3.1. Redesigning the SLA 3D printer

The current design of the Formlabs Form 2 (Somerville, MA, USA) SLA printer has 22.5×18 cm resin tank and 15×15 cm build platform which requires large quantity (125 mL) of material to optimize the desired resin to print one batch of MNs. Since the optimization process which involves the evaluation and processing of many batches to get the desired resin, the build platform and resin tank were reduced to 2×2 cm and 3×6 cm respectively to require less quantity of polymer and photoinitiator. The Formlabs Form 2 was redesigned using Autodesk Fusion 360 software (San Francisco, CA, USA). The stereolithography (STL) file was created with new dimensions of 6×3 cm and 2×2 cm for resin tank and build platform respectively. Further, the STL file was imported into the printer and was printed using clear resin. The printed structures were then washed in 70 % isopropyl alcohol (IPA) which were further cured in a Formlabs Form Cure UV Resin chamber (Formlab, MA, USA) for 1 hr at 60 °C. The final modified resin tank and build platform were fixed in the Formlabs Form 2 printer (Fig. 1).

2.3.2. Formulation of biocompatible resin for SLA 3D-printing

As shown in **Table S1** (in Supplementary File), Batches A1-A7 were formulated to assess their printability. Except Batch A1 and A2, in which LAP was directly added in PEGDAMA 550, in all other batches (A3-A7), LAP and methacrylated hyaluronic acid (Me HA) were first dissolved in water then added slowly into a beaker containing PEGDAMA 550. The resin was then kept on a hotplate stirrer at 42 °C for evaporation of water. The final resin was collected centrifuged for 5 min at 5000 rpm to

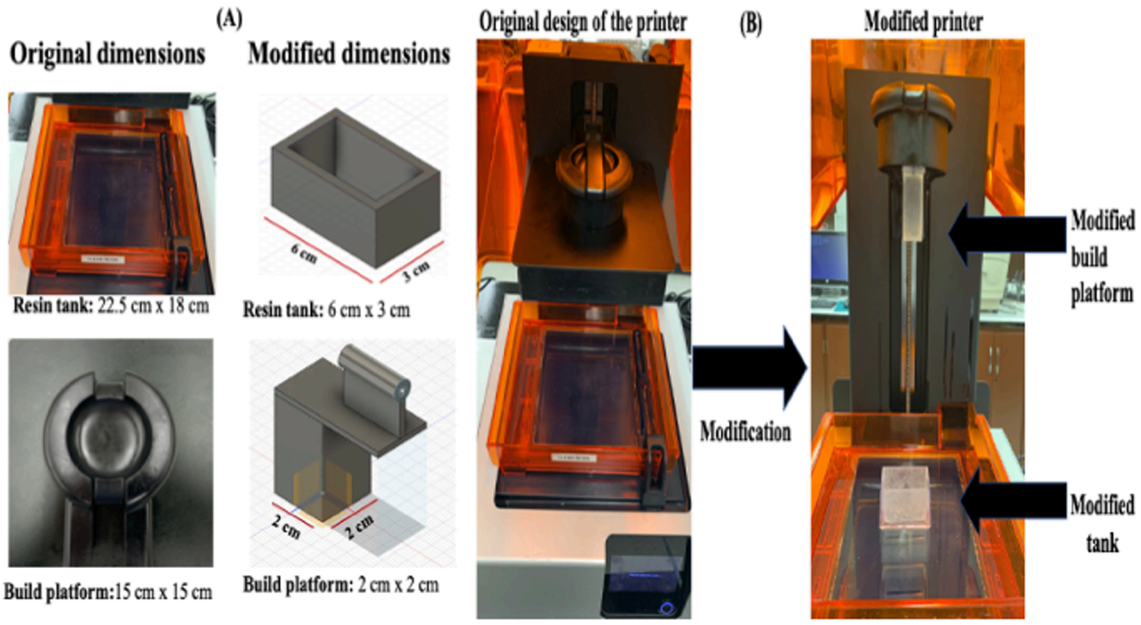

Fig. 1. (A) Redesigned Formlabs Form 2 SLA printer showing significant reduction in the size of build platform and resin tank in the modified printer. (B)Redesigned printer showing modified tank (6 cm × 3 cm) was fixed inside the large tank 22.5 cm × 18 cm) and the large build platform (15 cm × 15 cm) was replaced with small build platform (2 cm × 2 cm).

separate and remove undissolved particles. Clear supernatant was used for printing the MN patch.

2.3.3. SLA 3D-printing of microneedles patches

The STL file of a MN patch with 1000 μm space between each needle and dimensions of 600 μm height and 200 μm base diameter with a backing layer thickness of 2500 μm was created using Autodesk Fusion 360 (San Francisco, CA, USA) software. The STL file was imported into the Formlab printer using their PreForm software. The printed MN patch was washed in 70 % IPA and cured in a UV curing chamber for 15 min at 60 °C for hardness and durability. Morphology of 5 × 5 MN patch was then studied using Scanning Electron Microscopy (SEM) (Nova 400 NanoSEM, FEI, Hillsboro, OR, USA).

2.4. Formulation of biocompatible resin for DLP 3D-printing

Briefly, LAP was dissolved in water. LAP solution was then added in PEGDAMA 550 and vortexed for 1 min. IBU was then added and vortexed until it was completely dissolved in the resin. For Resins 3 and 4, LAP was dissolved in 20 %w/v of water which was then added in PEGDAMA 550 and vortexed for 1 min. Further, both Resins 3 and 4 were kept on hotplate stirrer at 42 °C for approximately 45–60 min for the evaporation of water. After the evaporation, 10 %w/v of water was left in both Resin 4 and 7. IBU was then added and vortexed until it completely dissolved in the resin (**Table S2**, Supplementary File). Solubility studies of IBU were conducted before optimizing the formulation. We observed that>8 %w/v IBU resulted in precipitation of IBU and turbidity in the formulation which suggests that 8 %w/v was the maximum amount of IBU soluble in our formulation. Therefore, 8 %w/v IBU was kept constant in the formulation.

2.5. Microneedle formulation optimization using design of experiment (DOE) quality by design

2.5.1. Preliminary screening of LAP concentration, water concentration, exposure time and light intensity

(A) Optimization of LAP and water concentration

Briefly, biocompatible PEGDAMA 550 resins with LAP concentration ranging from 0.11 to 0.75 %w/v in 10 %w/v water and 8 %w/v IBU were prepared (**Table S2** in Supplementary file). Resins with water concentration ranging from 10 to 30 %w/v with 0.23 %w/v LAP and 8 % w/v IBU were prepared (**Table S3** in Supplementary File). Resin was then poured in the resin tank and IBU MN patch was printed using 3D DLP printer. All the patches were tested for mechanical strength and morphological features including aspect ratio and tip Radius of Curvature (RoC).

(B) Optimization of Exposure Time and Light Intensity

Briefly, resins (Table 2 in Supplementary file) with LAP concentration ranging from 0.11 to 0.75 %w/v were printed at exposure time ranging from 1.5 to 8 *sec* and light intensity ranging (LED current) ranging from 100 to 150 (5.86 mA/unit). The printed IBU MN patch was evaluated for over polymerization and morphological features.

2.5.2. Design of experiment

IBU MN patch was optimized using three independent variables: LAP concentration (A), water concentration (B) and exposure time (C). A three-factor 2-response 20-run Central Composite Design was created where the aspect ratio and tip RoC of the MNs were measured. Statistics were analyzed by ANOVA using Design Expert v13(StatEase, Minneapolis, MN, USA) (Bagde et al., 2019a, 2019b; Kutlehria et al., 2020).

2.6. Optimization of print fidelity and needle Morphology using Artificial intelligence Machine learning programming

As shown in Fig. 2, the architecture of the Convolutional Neural Network (CNN) algorithm was used to assess the print fidelity and uniformity of the MN by examining the morphology of every needle in the path using a semi-supervised machine learning approach in the PyTorch platform. Briefly, the input layer consists of high-resolution microneedle images with a sample size of>500 images. 27 (three images from each QbD combination) of the 500 images were hand annotated to mark their category for classification. For this application, the data was categorized as training, testing and validation dataset with 70 percent of input image data for testing and the remaining 30 percent were classified as training and validation data. First, a CNN was pretrained in a supervised fashion using this labeled data. The self-learning approach was then used to predict the labels for the unlabeled data and utilize it for training. We utilized four hidden layers (one

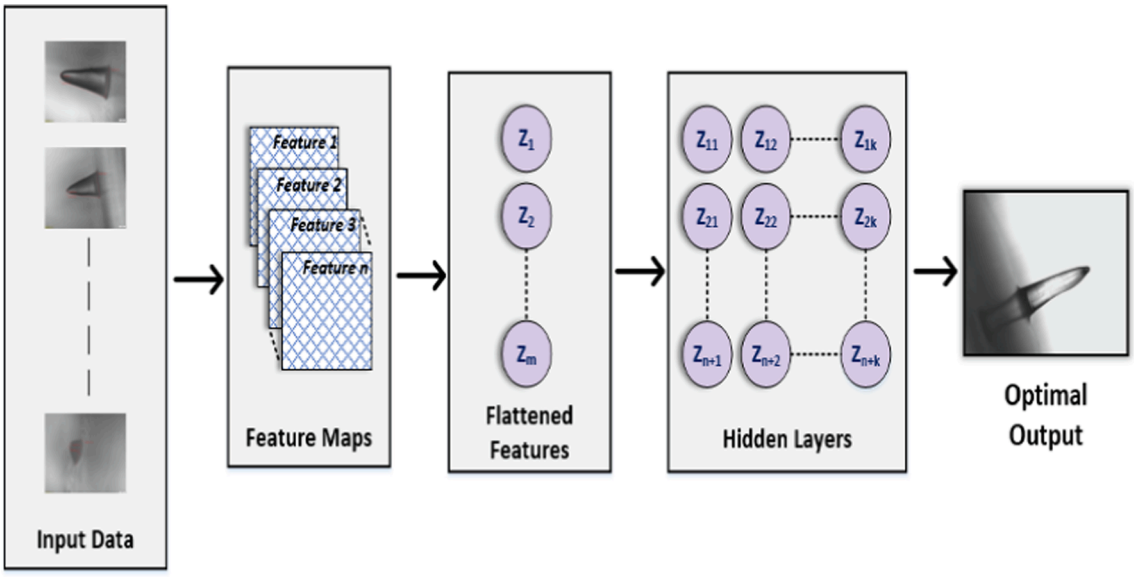

Fig. 2. Convolution neural network architecture for IBU MN optimization showing multiple steps to process the imaging data including feature maps, flattened features, hidden layers and finally optimal output.

convolutional layer, one pooling layer, one fully connected layer, and one normalization layer) with six hidden ReLU (Rectified Linear Units) were implemented. Four filters with 4 X 4 dimensions were used for feature extraction and normalization. For the given architecture of CNN, filters and their weights were used for model evaluation. In this approach, the CNN input raw pixels of an image and yields output as learned filter weights from the dataset. These weights serve input to the deep neural network for final prediction. The images were then classified by utilizing the flattened weighted feature maps obtained from the pooling layer (was used as input) and fully connected network of hidden layers (that computes the loss) and modifies the hidden layer weights.

Average pooling was done with a kernel size of 3 X 3 X 1. The classification was divided into nine output classes based on the microneedle morphology. The results were used as input for the needle morphological parameters in the QbD optimization process. The loss function for the self-learning is the same as that was used in the supervised learning. Finally, the new microneedle classifier obtained from the process above was evaluated with the testing data.

2.7. 3D DLP microneedle printing

The STL file of 10 × 10 MN patch was created using Autodesk Fusion 360. Further, it was sliced at 15 μm in the Kudo3D print job preparation software and imported into the Micro SLA DLP 3D printer. Optimized MN patches were printed at slice thickness of 25 μm, exposure time in the range of 4–5 *sec* and LED current of 125 (5.86 mA/unit). The printed MN patches were washed in 70 % IPA and cured in UV curing chamber at 23 °C for 15 min. Morphology of printed patch was then studied using SEM.

2.8. Mechanical strength

2.8.1. Parafilm M®-Based analysis

MN patch was pressed against multiple layers of wrapping film (Parafilm M® Laboratory film, Neenah, WI, USA) for 60 secs with manual thumb pressure of approximately 32 N per MN patch, and observed with an optical microscope to check if the pores are formed on the Parafilm M®. The mechanical strength of MNs was estimated from the pores formed on each layer (Nguyen and Banga 2017).

2.8.2. Texture analysis

Briefly, MN patch was attached to the moving probe (TA XT Texture Analyzer, Stable-Micro Systems, USA) using adhesive tape. The patch was then pressed against the human dermatomed skin on a flat aluminum block with a compression force of 0.1, 0.2, 0.3, 0.4 and 0.5 N/needle for 30 *sec* at a rate of 0.5 mm/*sec*. Pre-test and post-test speed were set at 0.5 mm/*sec*. MN height was measured before and after applying the force and change in height or any deformation was recorded (Migdadi et al., 2018).

2.9. In vitro release testing

MN patch was added in 20 mL of phosphate buffer (pH 7.4) with 25 %v/v ethanol and 5 %v/v Tween 80 in a beaker and kept on magnetic hotplate at 350 rpm at 37 °C. Samples were taken at 0.25, 0.5, 1, 2, 3, 4, 5, 6, 12 and 24 hr. At each sampling time, fresh 20 mL of phosphate buffer was replaced in the beaker (Johnson et al., 2016). Further, all the samples were analyzed using HPLC with 70 % acetonitrile (ACN) and 30 % acidified water (pH 2.5 adjusted using o-phosphoric acid), injection volume 50 μL and flow rate 1 mL/min at 221 nm wavelength using a previously validated method (Bagde et al., 2019a, Palekar et al., 2022). MN patches were also examined with the optical microscope at 2, 5 and 24 hr to evaluate the effect of release media on the morphology of MNs and to understand the release mechanism.

2.10. Ex vivo permeation testing through human skin

Dermatomed human skin [0.5 ± 0.1 mm thickness] was purchased from New York Firefighters Skin Bank (New York Presbyterian Hospital, NY, USA) and transported in 10 % glycerin solution in saline and stored at −80 °C. The skin was defrosted and rinsed with distilled water for 15–20 min to remove excess glycerin before all experiments. Our laboratory has previously validated the methods of storage and preparation of dermatomed human skin and has certified that the skin retains its integrity for accurate permeation. The receiver compartment comprised of (pH 7.4) PBS buffer with 25 %v/v ethanol and 5 %v/v Tween 80 and was maintained at 32 ± 0.5 °C with continuous stirring at 300 rpm. Briefly, MN patch was placed on the skin with manual thumb pressure. Sellotape was then placed on top of the patch to maintain MN contact with the skin. The skin with the patch was then mounted between the donor and receiver compartments of Franz diffusion cells (PermeGear

Inc., Riegelsville, PA, USA). Samples were taken at 24, 48 and 72 hr in triplicate. At each sampling time, fresh release media was replaced in the receiving compartment (Fulzele et al., 2007).

2.11. In vivo pharmacokinetic (PK) collection

Sprague–Dawley male rats weighing about 250 g were used to evaluate transdermal performance of MN in vivo The animals were acclimatized to laboratory conditions for 7 days before the experiment. To prevent fur from interfering with dermal contact of the patch, animals were anesthetized using 2–4% isoflurane in oxygen, 24h before experimentation, and the hair was removed with an animal hair clipper. Briefly, animals were divided into 2 groups: 0.23 %w/v LAP + 10 %w/v water (Group 1) and 0.49 %w/v LAP + 10 %w/v water (Group 2). 2 patches with size of 1.5 × 1.5 cm with 100 MNs were applied on rat to deliver IBU transdermally. IBU MN patches were adhered on the back of the SD rats (N = 4) with the help of 3 M Tegaderm™ adhesive patch. Blood samples were collected at 1, 2, 4, 6, 8, 12, 24 and 48 hr time intervals. Plasma was separated from whole blood samples by centrifuging them at 4000 rpm at 4 °C. Plasma samples were then stored at −80 °C until they were analyzed (McCrudden et al., 2014). All the samples were analyzed using HPLC with 90 % ACN and 10 % acidified water (pH 2.5 adjusted using o-phosphoric acid), injection volume 60 µL and flow rate 0.5 mL/min at 221 nm wavelength. At the end of the study, rats were examined for any inflammation or damage caused by patch application on the skin (Bagde et al., 2019a).

2.12. Statistical and PK analyses

All raw data results have been expressed as the mean ± standard deviation for at least three repetitions. Two-way analysis of variance (ANOVA) analysis was used for the comparison among multiple groups followed by Tukey's Multiple Comparison Test whereas student's *t*-test analysis was used for the comparison between two groups. The mean differences were considered significant in all experiments valued at *p < 0.05, **p < 0.01 and ***p < 0.001. Pharmacokinetic analyses were carried out using PKSolver and Graphpad Prism (Dotmatics, Boston, MA, USA), for noncompartmental analysis and user-defined model fits, respectively (Zhang et al., 2010). Model fit parameters were reported as mean ± standard error. An in-vitro in-vivo relationship was evaluated by calculating the fraction absorbed in vivo using the Wagner-Nelson method of numerical deconvolution (Wagner and Nelson 1964).

3. Results

3.1. MNs using redesigned SLA 3D-Printing technology

As shown in the Fig. 1 the redesigned Formlab printer with a resin tank of 3 × 6 cm and build platform of 2 × 2 cm) was able to print the MN patch with 10 mL resin which was significantly less compared to 125 mL resin required in the Formlabs Form 2 printer.

Batches A1-A4 were not able to polymerize for production of MN patches. Batches A5-A6 containing Me HA were able to polymerize and print the backing layer of the MN patch but not the MNs. However, Batch 7 resin containing high concentration of LAP and Me HA compared to Batches A5-A6 printed 5 × 5 MN patch using the redesigned Formlab printer. SEM images of Batch 7 showed revealed a MN measuring ~ 400 µm in height, ~ 370 µm in base diameter and ~ 30 µm in tip RoC. Images also revealed that surface of MN and backing layer was wavy and rough (Fig. 3).

3.2. DLP 3D-Printed microneedles

3.2.1. Formulation optimization

A) Optimization of LAP Concentration.

IBU MN patches printed using Resin 2, 3 and 4 could form pores on the Parafilm M®. However, Resin 1 with LAP concentration of 0.112 % w/v produced brittle MNs which broke off when pressed against Parafilm M®. Therefore, LAP concentration in the range of 0.23–0.75 %w/v was selected for the design of the experiment.

B) Optimization of Water Concentration.

Parafilm M® Our results showed that Resin 8 with water concentration of 40 %w/v produced over polymerized and brittle patches. Moreover, patches with water concentration ≥ 30 %w/v produced IBU MN patches hazy in appearance compared to patches with water concentration ≤ 20 %w/v. Therefore, water concentration in the range of 10–30 %w/v was selected for the design of the experiment.

(C) Optimization of Exposure Time and Light Intensity

IBU MN patches printed with the exposure time in the range of 1.5–8 *sec* didn't show over-polymerization when printed at LED current of 125 (5.86 mA/unit), however when increased to 150 (5.86 mA/unit), MNs showed over-polymerization. Moreover, when the LED current was decreased to 100 (5.86 mA/unit), MNs were not printed. Therefore, all MN patches were printed at LED current of 125 (5.86 mA/unit). Prior to statistical optimization, preliminary results suggested that resins with LAP concentration < 0.23 %w/v at LED current of < 120 and exposure time of ≤ 1 *sec*, printed short MNs < 600 µm height, >350 µm base diameter and > 30 µm tip RoC.

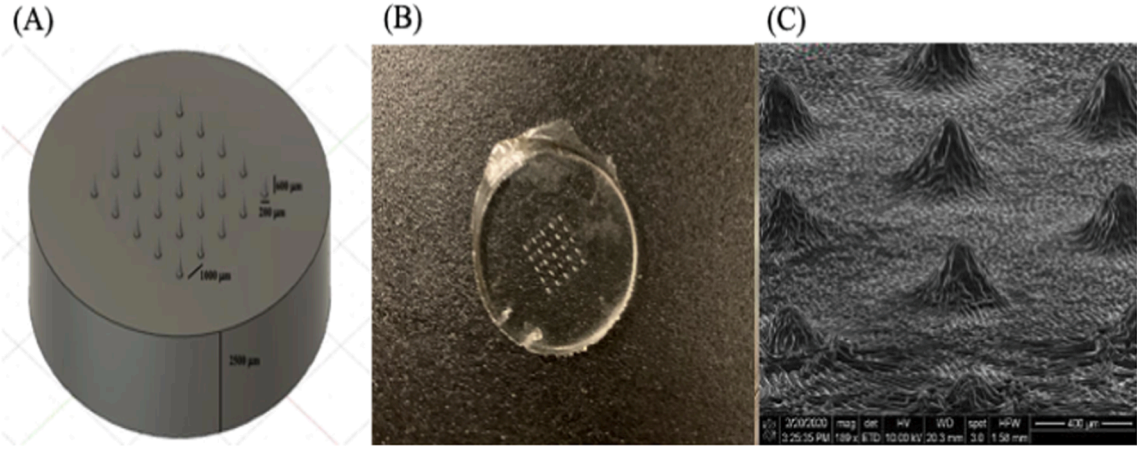

Fig. 3. (A) STL file created using Autodesk Fusion 360 software showing 600 µm height, 200 µm base diameter and 1000 µm space between two needles and 2500 µm backing layer thickness. (B) 5 X 5 MN patch showing the needles are printed on the backing layer. (C) SEM image of 5 X 5 MN patch showing MNs with height of ~ 400 µm, base dimeter of ~ 370 µm and tip RoC of ~ 30 µm.

3.3. Design of experiment (DOE)

A cubic model was found to be aliased for both aspect ratio and tip RoC where the lower order quadratic model was found to have best fit. From ANOVA, it was observed that the independent variables for LAP concentration (A), exposure time (C), A^2 and C^2 significantly affected the aspect ratio whereas, A, C, BC and C^2 significantly affected the MN tip RoC. Data showed that water concentration ($p < 0.0001$) and exposure time ($p < 0.05$) affected both the aspect ratio and RoC of MN tip. When the water concentration was increased, aspect ratio was decreased and RoC was increased. Whereas when the exposure time was increased, aspect ratio was decreased and RoC was increased.

Optimization of IBU MN was based on response surface analysis following combination of response parameters into an objective function, i.e., a desirability function in the range of 0 to 1 for worst response parameters to best response parameters. respectively. The batch with highest desirability was selected for the prediction of responses of the model. Further, the optimized formulations were repeated three times and the results were compared with predicted responses. Data showed no significant difference between the predicted and experimental values. Four batches including 1) LAP 0.23 %w/v and 10 %w/vwater 2) LAP 0.23 %w/v and 20 %w/v water 3) LAP 0.49%w/v and 10 %w/v water 4) LAP 0.49 %w/v and 20 %w/v water were selected as optimized batches for further studies (Fig. 4**A, B, C and D and** Table 1**A, B and C**).

3.4. Artificial Intelligence: Machine learning evaluation

In evaluating print fidelity and needle morphology, it was observed that aspect ratio and RoC of batches 1 to 4 which include LAP (0.23 %w/v) + water (10 %w/v), LAP (0.23 %w/v) + water (20 %w/v), LAP (0.49 %w/v) + water (10 %w/v) and LAP (0.49 %w/v) + water (20 %w/v) were ~ 3 and ~ 15 μm respectively. As we see in the Fig. 4**E**, the image analysis algorithm yields a good learning curve for the final model selected. A decreasing training and validation loss was used as input to the QbD for optimal prediction for the IBU MN patches (Fig. 4**E and** Table 2).

3.5. DLP 3D-Printing of Ibuprofen-Loaded microneedles

Resin formulations including 1) LAP 0.23 %w/v and 10 %w/v water 2) LAP 0.23% w/v and 20 %w/v water 3) LAP 0.49 %w/v and 10 %w/v water 4) LAP 0.49 %w/v and 20 %w/v water produced prominent MN patches with no over polymerization when printed at 25 μm slice thickness, LED current of 125 (5.86 mA/unit) and exposure time in the range of 4–5 *sec*. SEM images showed that MNs were fabricated with a height of ~ 750 μm height, ~250 μm base diameter and tip with RoC of ~ 15 μm (Fig. 5).

3.6. Mechanical properties of ibuprofen microneedles

3.6.1. Parafilm M®-Based analysis

IBU MN patches printed using Resin 5, 6 and 7 were mechanically strong enough to form pores on the Parafilm M®. After applying IBU MNs on the Parafilm M®, conical pores were formed on both 1st and 2nd layer of the Parafilm M®. Furthermore, 3rd layer showed indentation created by MNs. Images also showed that pores formed on the Parafilm M® were distinct and uniform in shape and size which suggests that IBU MNs were strong enough to break the epidermal layer of skin (Fig. 6**A**).

3.6.2. Texture analysis

Data showed that when IBU MN patch was pressed against the dermatomed human skin using a movable probe at different force in the range of 0.1–0.5 N per MN, height of the MNs was not decreased which suggests that MNs are strong enough to perforate the skin. Optical microscopic images also confirmed that IBU MNs didn't break even after applying high force of 0.5 N per MN (Fig. 6**B, C and D**).

3.7. In vitro release testing

In vitro drug release data showed > 70 % drug was released in the

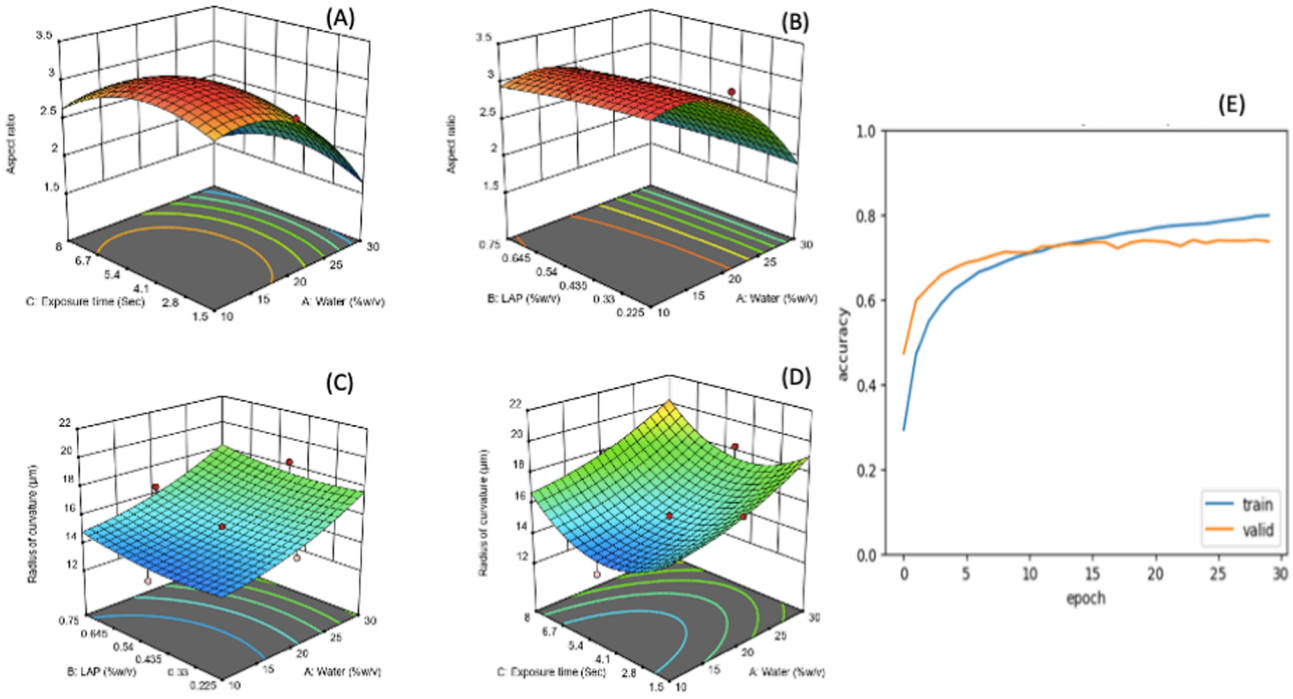

Fig. 4. (A) 3D plot showing the effect of exposure time and water concentration on aspect ratio of the IBU MNs, (B) 3D plot showing the effect of LAP and water concentration on aspect ratio of the IBU MNs, (C) 3D plot showing the effect of LAP and water concentration on RoC of the IBU MNs, (D) 3D plot showing the effect of exposure time and water concentration on RoC of the IBU MNs, (E) Validation of DOE by Artificial Intelligence (AI) and machine learning algorithms showing decreasing training and validation loss.

Table 1
(A) Central composite design showing 20 different batches with 5 center points and their results, (B): Factors in DOE after applying the constraints, (C): Point prediction from the DOE after applying the constraints.

(A)

Run	Factor 1 A: Water	Factor 2 B: LAP	Factor 3 C: Exposure time	Response 1 Aspect ratio	Response 2 Roc
	%w/v	%w/v	Sec		µm
1	20	0.49	1.5	2.83	16.9
2	30	0.75	8	1.52	21.58
3	20	0.49	4.75	2.94	15.21
4	20	0.49	4.75	2.94	15.21
5	10	0.75	1.5	2.88	15.6
6	20	0.75	4.75	2.89	16.5
7	20	0.23	4.75	3.17	14.8
8	30	0.23	1.5	1.59	19.99
9	20	0.49	4.75	2.94	15.21
10	10	0.23	8	2.78	16.23
11	20	0.49	4.75	2.94	15.21
12	30	0.75	1.5	1.62	18.68
13	10	0.75	8	2.37	18.58
14	10	0.49	4.75	3.18	13.22
15	20	0.49	4.75	2.94	15.21
16	10	0.23	1.5	2.78	17.2
17	20	0.49	8	2.68	17.83
18	20	0.49	4.75	2.94	15.21
19	30	0.49	4.75	1.95	18.33
20	30	0.23	8	1.53	19.56

(B)

Factor	Name	Batch 1	Batch 2	Batch 3	Batch 4
A	Water concentration (%w/v)	10.00	20.00	10.00	20.00
B	LAP concentration (%w/v)	0.23	0.23	0.49	0.49
C	Exposure time (sec)	5.06	5.03	4.39	4.33

(C)

Batch	Response	Predicted mean	Observed mean
Batch 1	Aspect ratio	3.127	3.09
	Radius of curvature (µm)	14.176	14.41
Batch 2	Aspect ratio	3.010	2.97
	Radius of curvature (µm)	15.33	15.62
Batch 3	Aspect ratio	3.079	2.92
	Radius of curvature (µm)	14.03	14.59
Batch4	Aspect ratio	2.994	2.91
	Radius of curvature (µm)	15.17	15.58

Table 2
Validation of DOE using AI algorithms showing no significant difference in aspect ratio and Tip RoC of optimized batches.

Batch	Factor 1 A: Water (%w/v)	Factor 2B: LAP (%w/v)	Factor 3C: Exposure Time (*Sec*)	Response 1 Aspect Ratio	Response 2 Radius of Curvature (µm)
Batch 1	10	0.225	5.07	3.10	14.44
Batch 2	20	0.225	5.02	2.96	15.72
Batch 3	10	0.49	4.41	2.93	14.64
Batch 4	20	0.49	4.32	2.91	15.39

first 12 h from all the IBU MN patches including 1) LAP 0.23 %w/v and 10 %w/v water 2) LAP 0.23 %w/v and 20 %w/v water 3) LAP 0.49 %w/v and 10 %w/v water 4) LAP 0.49 %w/v and 20 %w/v water. Furthermore, all the patches showed > 75.00 % drug release in 24 hr. Results also showed no significant difference in drug release profile among IBU MN patches containing 10 %w/v and 20 %w/v water or LAP 0.23 %w/v and 0.49 %w/v. SEM images clearly showed that MNs were dissolved in the phosphate buffer over the period (Fig. 7). Microscopic images demonstrated that MN base diameter was increased from ~ 250 µm to ~ 320 µm with decrease in height from ~ 750 µm to ~ 600 µm after 2 h with slight swelling. Further increase in dissolution with decrease in the height of MNs was observed at the end of 5 hr. IBU MNs were then examined in SEM and images showed that MNs were dissolved in release media with significant height reduction to ~ 100 µm at the end of 24 h. The in vitro release profile displayed a best fit (i.e. using AIC Information Criterion and F-test) (Fig. 1 in Supplementary file) to a combination First Order/Zero Order Model with Lag Time as shown below in the **Equation X where Ko is the zero-order rate and Kr is the first order release constant**. The parameters for the in vitro release model are shown in Table 4 in Supplementary file.

$$\%\,Released = 100^{*}\left(1 - e^{-Kr^{*}t}\right) + Ko^{*}(Tlag - t) \quad (X)$$

3.8. Ex vivo permeation testing through human skin

Our results revealed that IBU MN patches with 0.23 %w/v LAP and 10 %w/v water showed 1864.39 ± 231.49 µg/cm^2 drug permeation which was significantly higher ($p < 0.01$) as compared to patches containing 0.23 %w/v LAP and 20 %w/v water which showed 1069.63 ± 204.67 µg/cm^2 at the end of 72 h study. Similarly, IBU MN patches with 0.49 %w/v LAP and 10 %w/v water showed 2008.15 ± 358.12 µg/cm^2 which was significantly higher ($p < 0.01$) as compared to patches containing 0.49 % LAP and 20 % water which showed 1104.35 ± 248.39 µg/cm^2 at the end of 72 h study. IBU MN patch containing 0.23 %w/v LAP and 10 %w/v water showed flux of 40.46 ± 5.02 µg/cm^2/h whereas IBU MN patch containing 0.23 %w/v LAP and 20 %w/v water showed

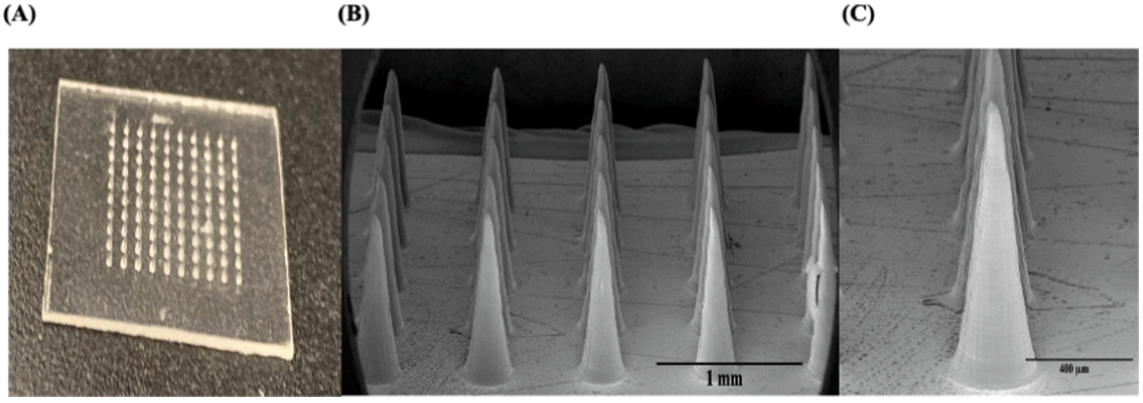

Fig. 5. (A) 4 cm^2 IBU MN patch after finishing the printing. (B) SEM image of IBU MN patch showing prominent MNs with height of ~ 750 µm height, 350 µm base diameter and 15 µm tip RoC (C) Magnified view of one row of IBU MN array.

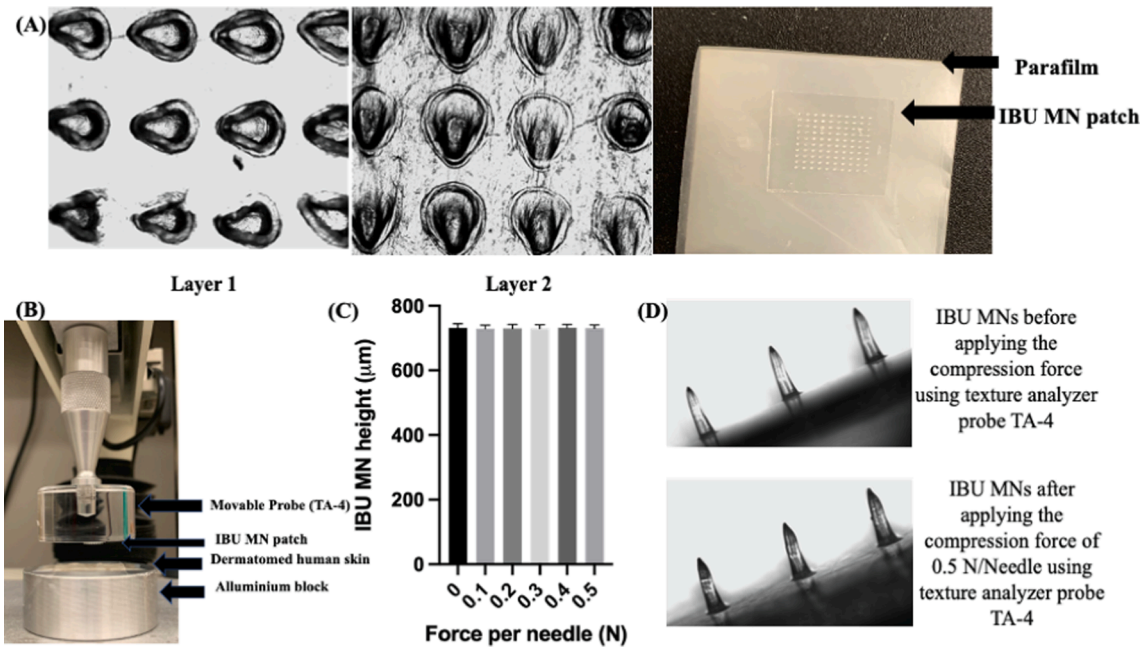

Fig. 6. (A) Pores formed on the parafilm after applying slight thumb pressure showing the significant mechanical strength of IBU MN patch to pierce into the skin layers (B) Moving texture analyzer probe with MN patch attached at the bottom and aluminum block with dermatomed skin mounted on top of it (C) Effect of force applied on height of MNs showing no effect on height change. (D) Optical microscopic images of MNs before and after applying the force showing no deformities in MNs after pressing against the skin.

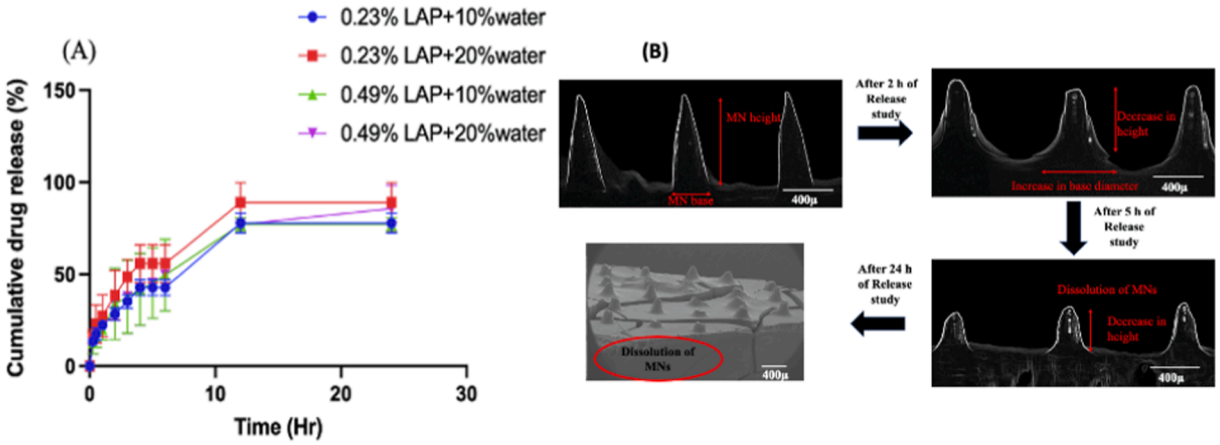

Fig. 7. (A): IVRT study showing no significant effect in percent drug release from IBU MN patches containing 0.23 %w/v LAP + 10 %w/v water, 0.23 %w/v LAP + 20 %w/v water, 0.49 %w/v LAP + 10 %w/v water, and 0.49 %w/v LAP + 20 %w/v water. (B): IBU MNs showing increase in base diameter with decrease in height followed by significant dissolution of MNs over the period of 24 hr in in vitro release study.

flux of 23.21 ± 4.44 μg/cm^2/h. Similarly, IBU MN patch containing 0.49 %w/v LAP and 10 %w/v water showed flux of 43.58 ± 7.77 μg/cm^2/h whereas IBU MN patch containing 0.49 %w/v LAP and 20 %w/v water showed flux of 23.97 ± 5.39 μg/cm^2/h (Fig. 8).

3.9. *In vivo pharmacokinetic study*

Results revealed that IBU MN patches containing 1) 0.23 %w/v LAP with 10 %w/v water and 2) 0.49 % w/v LAP with 10 %w/v water showed 3745.76 ± 897.67 ng/ml and 3288.18 ± 548.30 ng/ml systemic absorption respectively at about 2 h. Moreover, 1000 ng/ml IBU plasma concentration was maintained for 48 h for both the groups. Data also showed 62812.02 ± 11128.39 (ng/ml*h) of AUC (0–48 h) for IBU MN patch containing 0.23 %w/v LAP with 10 %w/v water and 58415.53 ± 19781.56 (ng/ml*h) for IBU MN patch containing 0.49 %w/v LAP with 10 %w/v water. It was observed that at the end of the study, the IBU MN patches were strongly adhered to the rat's skin. No inflammation or damage was observed on the rat's skin at the end of the study (Fig. 9). The plasma concentration versus time profiles were fit to a Parallel First Order / Zero Order Input, One Compartment Model, according to the **Equation Y** below, where Ke is the reference elimination constant for ibuprofen in rats, Ko is the zero-order input rate and Ka is the first order absorption constant (Fig. 2, **Supplementary Data**).

$$Plasma\ Ibuprofen\left(\frac{ng}{mL}\right) = \frac{D_{Abs}}{V} * \frac{Ka}{(Ka - Ke)}\left(e^{-Ke*t} - e^{-Ka*t}\right) + \frac{Ko}{Ke} * (1 - e^{-Ke*t}) \quad (Y)$$

The model adequately describes the combined mechanism of drug input into the animals and provides derived PK parameters in the Table 5 in Supplementary Data. Given the unknown dose administered or remaining in the patch, here an estimate of the dose absorbed from the

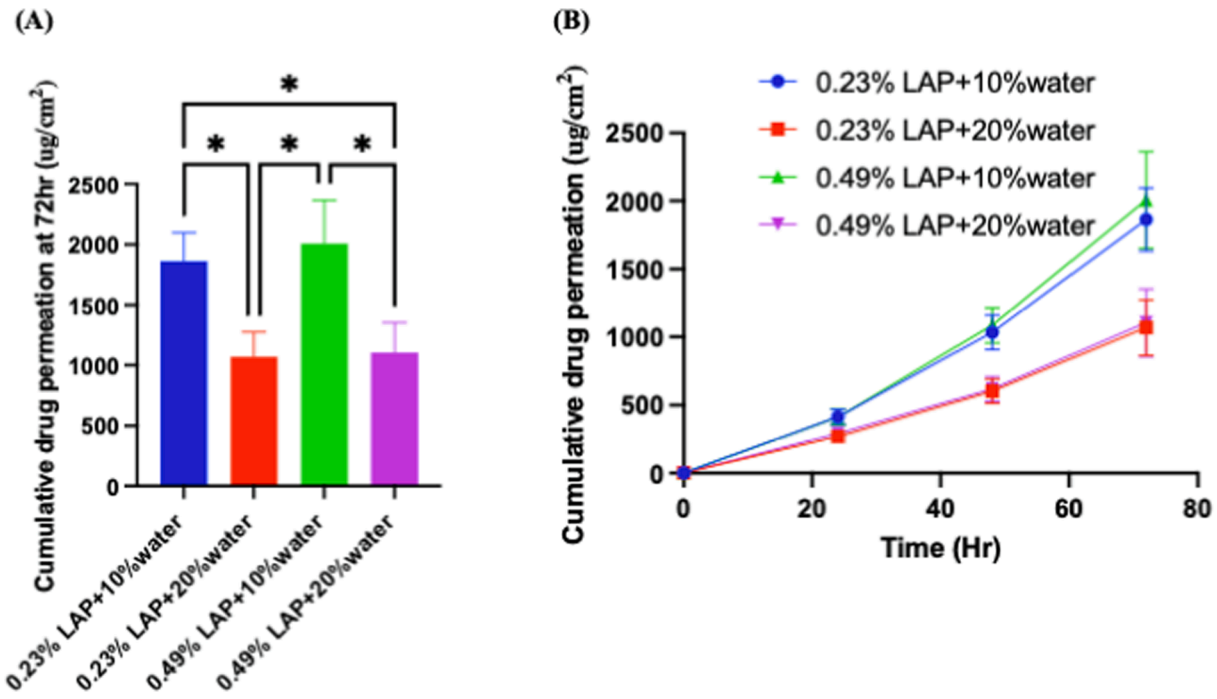

Fig. 8. (A)IVPT study showing 0.22 % LAP + 10 % water and 0.49 % LAP + 10 % water showed higher drug permeation compared to 0.22 % LAP + 20 % water and 0.49 % LAP + 20 % water at the end of 72 hr. (B) IVPT study showing 0.22 % LAP + 10 % water and 0.49 % LAP + 10 % water showed significantly high cumulative drug permeation at 24, 48 and 72 hr compared to 0.22 % LAP + 20 % water and 0.49 % LAP + 20 % water.

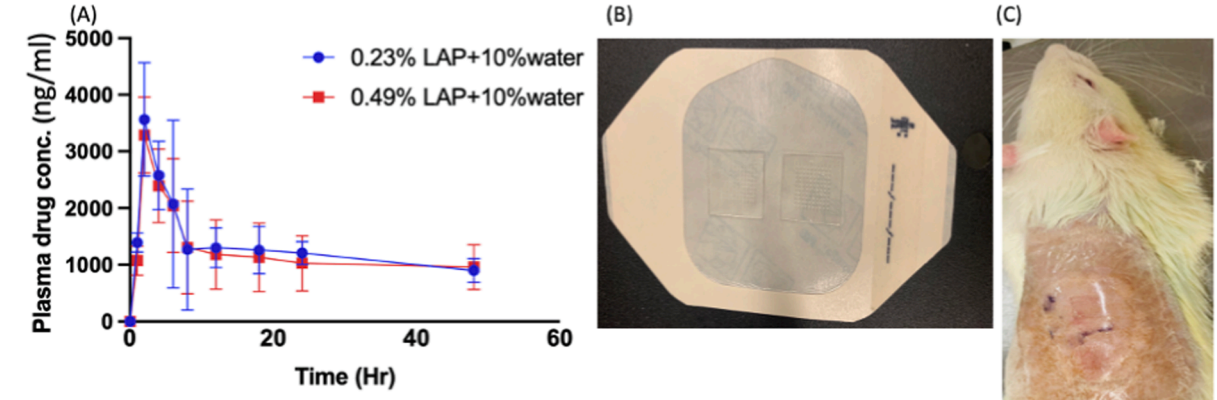

(D)

	AUC (0-48 hr) (ng/ml*hr)	Tmax (hr)	Cmax (ng/ml)
IBU MN patch (0.23%LAP+10% water)	62812.02 ± 11128.39	2.66 ± 1.12	**3717.43 ± 782.25**
IBU MN patch (0.49%LAP+10% water)	58415.53 ± 19781.56	2.00 ± 00	**3288.18 ± 548.30**

Fig. 9. (A) PK study of IBU MN patch on Sprague dawley rats showing no significant effect in systemic absorption of IBU from the IBU MN patches containing 0.23 % w/v LAP + 10 %w/v water and 0.49 %w/v LAP + 10 %w/v water. (B) IBU MN patches on the tegaderm transparent adhesive film to adhere on back of rats. (C) SD rat with IBU MN patch adhered on back. (D) PK parameters of IBU MN patches at the end of 48 hr study.

PK model was calculated.

3.10. In Vitro-In vivo relationship

Results from the IVIVR analysis yielded the fraction absorbed at each time point (Fig. 10) and the percent absorbed in vivo versus the percent released in vitro (Figs. 2, 3 and 4 in Supplementary Data). Given that at a 1:1 correlation, the difference between in vitro and in vivo fraction absorbed are nil, and this difference is at the root of the F1 and F2 difference and similarity factors respectively, we modeled the difference at each time point to yield the 2nd order polynomial regression equation which can predict the fraction absorbed for every fractional unit of in vitro release with an $R^2 = 0.98$. Although this model was performed in Excel, the polynomial IVIVR relationship is also commercially available in IVIVC software, such as GastroPlus software (Simulations Plus, USA).

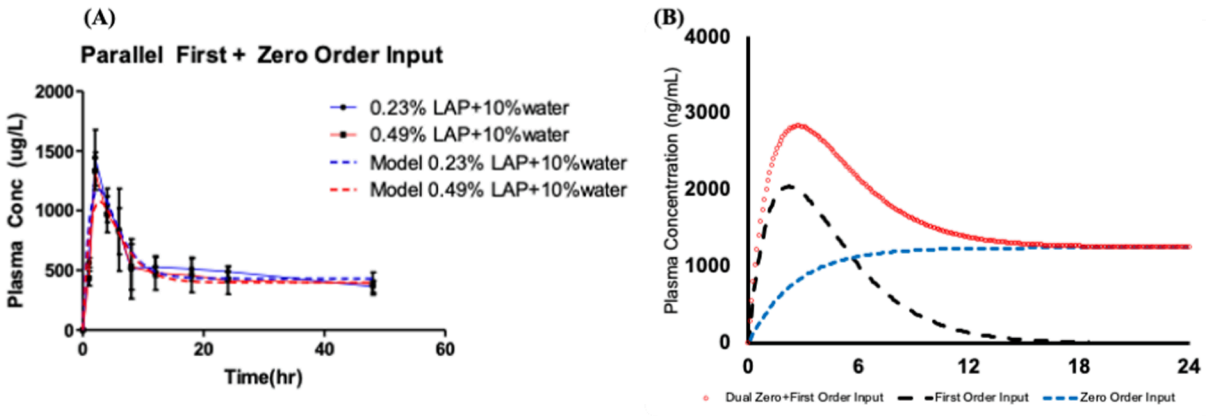

Fig. 10. IVIV correlation study of IBU from the IBU MN patches containing 0.23 %w/v LAP + 10 %w/v water and 0.49 %w/v LAP + 10 %w/v water showing rapid dual mechanism of input with a rapid first order input phase and parallel zero order input.

4. Discussion

There are limited reports published on 3D printed microneedles for evaluation of transdermal delivery and absorption of small molecules. Since the 3D printing technique bypasses multiple steps involved in conventional micromolding techniques, our objective was to first develop the custom resin, compatible for both DLP and SLA 3D printing technology and to print sharp dissolvable microneedles (using QbD supplemented by AI approach) and to evaluate the optimized IBU MN patches in in vitro and in vivo studies.

Our results showed that resin use was reduced by 12.5-fold in redesigned Formlab SLA printer compared to original design to process one batch of resin. Using the redesigned printer, various batches were processed with different compositions to print the MNs. Manzano et al. have demonstrated screening multiple resins by building a high throughput block adaptor (HTB) in SLA 3D printer. In this study, HTB was used to test printability of multiple resin compositions in significantly less time per print (<1/16 based on a 4 × 4 matrix) with less resin quantity (<2 mL) than using the original hardware (Manzano et al., 2019). This study supports our modified design of SLA printer which was used to fabricate dissolvable MNs. This increases throughput when testing multiple polymer combinations for their impacts on polymer dissolution and drug release rates for different molecules.

Data from our experiments demonstrated that Batch 7; clear transparent resin with high concentration of LAP and Me HA printed 5 × 5 MN patch using SLA printer. As expected, the concentration of LAP and Me HA had a significant effect on MN printing. Than et al. demonstrated that Me HA could help MNs in maintaining its structural integrity and mechanical strength (Than et al., 2018). This study demonstrated fabrication of dissolvable MNs using SLA technology and a biocompatible resin with LAP as a photoinitiator which is cyto-compatible. However, the SLA printer produced MNs with height<450 μm, base diameter of about ~ 370 μm and ~ 30 μm in tip RoC. Even after importing STL file with MN dimensions of 600 μm height, 200 μm base diameter and 25 μm tip diameter, the desired MN patch was not able to be printed due to its xy-directional resolution. Moreover, light intensity, exposure time and slice thickness couldn't be controlled in SLA printer. We therefore proceeded to use DLP technology because of its various advantages including high printing speed compared to SLA printing and control over layer-by-layer printing with more accuracy and precision. Although significant work was performed with SLA printing, the authors moved to DLP technology mostly because the specifications required for MNs was not met due to lower resolution of the SLA printer. The authors however would like to point out that the work demonstrated here shows the possible modifications we can make with the SLA printer to save on resin cost, and also MNs which could be used for other applications in future.

Using the DLP technology, we successfully developed a resin formulation containing LAP as a photoinitiator in PEGDAMA (MW 550) loaded with IBU resulting in observably sharp microneedles with SEM. Although, LAP has been reported in many studies as a crosslinking photoinitiator, it is poorly soluble in PEGDAMA (unlike TPO and BAPO) and its solubility in water is about ~ 0.25 %w/v. To overcome the poor solubility of LAP in PEGDAMA, it was first dissolved in water and then added into PEGDAMA while developing the resin formulation. Pre-optimization results suggested that resins with LAP concentration < 0.23 % w/v at LED current of < 120 and exposure time of ≤ 1 *sec*, printed short MNs with < 600 μm height, >350 μm base diameter and > 30 μm tip RoC. QbD results revealed that water concentration and exposure time significantly affected IBU MNs configuration. When water concentration was increased above 20 %w/v, aspect ratio significantly ($p < 0.0001$) decreased, and RoC significantly ($p < 0.0001$) increased. Further, it was observed that exposure time above 5 *sec* resulted in a significant decrease ($p < 0.05$) in aspect ratio and significant increase ($p < 0.05$) in RoC. SEM images revealed that DLP printed IBU MNs with height of ~ 750 μm, base diameter of ~ 350 μm and tip RoC of ~15 μm. Lim et al. (2021) also fabricated MN arrays using DLP printing with height of 800 μm, tip diameter 100 μm, interspacing 800 μm and base diameter of 400 μm. However, the geometry of the MN was not be able to penetrate the skin consistently because of the large tip diameter of 100 μm (Lim et al., 2021). This study provides observational evidence that that exposure time plays a crucial role in printing MNs with sharp tips and a high aspect ratio, and is consistent with our previous findings (Kundu et al., 2020).

The optimal parameters obtained using AI for needle morphology and print fidelity were used as one of the input parameters for QbD optimization of IBU MN to obtain DOE results of optimization of IBU MN patch. Aksu et al. has also reported the application of AI along with QbD approach for manufacturing of ramipril tablets by direct compression method (Aksu et al., 2012). Overall, we sought to demonstrate the value and utility of saving time, raw materials, and improving results through the AI machine learning coupled with QbD DOE approach. Mechanical strength studies showed that MNs with LAP concentration in the range of 0.23–0.49 %w/v had sufficient mechanical strength (which was enough to form pores in skin). However, LAP concentration < 0.23 %w/v resulted in soft and brittle MNs suggesting that LAP concentration plays important role to make the MNs strong enough to pierce the skin. Our DLP printed IBU MNs formed holes on the Parafilm M® film after applying slight thump pressure suggesting that MNs were sufficiently strong to break the stratum corneum layer of the skin. Nguyen et al. reported that maltose MNs when evaluated for mechanical strength on Parafilm M® film, pores were formed on it showing their strength to pierce the human skin (Nguyen and Banga 2017). Additionally, texture analysis on MNs strength showed that IBU MNs didn't show any deformation in their morphology at force applied in the range of 0.1–0.5

N per MN which suggests that MNs are strong enough to perforate the skin. It is also reported that about 25–35 N force is required for MN to pierce the skin depending on the sharpness of the MNs (Cheung et al., 2014, Larrañeta et al., 2014, Lutton et al., 2015, Migdadi et al., 2018).

In vitro release study results revealed that the percent water composition did not have any statistically significant impact on ibuprofen release, as both 0.23 %w/v LAP with 20 %w/v water and 0.49 %w/v LAP with 20 %w/v water IBU MN patches had release profiles comparable to 0.23 %w/v LAP with 10 %w/v water and 0.49 %w/v LAP with 10 %w/v water. The possible mechanism in dissolving of MNs was initial increase in base diameter of MNs because of absorption of release media (due to the porosity of the PEGDAMA) which resulted in slight swelling of MNs. This might have contributed to increased diffusion of a drug from MNs into the release media compared to the in vivo situation since the patches were completely immersed in the release medium with constant stirring. These findings are consistent with Nguyen et al. who developed dissolvable poly (vinyl alcohol) MNs using micromolding technique for transdermal delivery of doxorubicin and showed significantly high release of doxorubicin from dissolving MNs (Nguyen et al., 2018). Similarly, Lim et al. reported in vitro release using a DLP printed MN array fabricated with PEGDA and VP (7:3) resin composition, and showed over 70 % drug release in the first 5 hr (Lim et al., 2021). Based on visual observation of the percent released versus time profile, there appeared to be an instant or burst release profile followed by a more sustained linear release rate with time, as described previously (Welling, 1983). The in vitro data was successfully fitted to a combination of first and zero order release model with a zero-order lag time parameter. The lag time parameter was required, and did not show up in vivo observations, likely due to the plasma elimination of ibuprofen with a relatively short half-life (i.e. $\approx$ 1.8 h in rats). The second phase of predominantly zero order release can be explained due to completion of a burst phase after given the first order release constant of$<$0.15/hr yielding a first order release half-life of under 4.6 h.

Data from ex-vivo permeation in human skin in this study revealed that 0.23 %w/v LAP with 10 %w/v and 0.49 %w/v LAP with 10 %w/v water showed substantially higher (almost 2-fold increased) permeation at 72 h compared to 0.23 %w/v LAP with 20 %w/v water and 0.49 %w/v LAP with 20 % w/v water. Considering that in vitro release in media did not show water dependency, we conclude this inverse relationship between water concentrations in the resin formulation and non-polar small molecule skin permeation could potentially be due to ibuprofen increasing its own permeation through human skin from saturated solutions, which has been reported by Al-Saidan (2004).

The pharmacokinetic in vivo evaluation showed that IBU was absorbed in the blood (Cmax = 3717.43 $\pm$ 782.25 ng/ml) from MNs which supported other data indicating that DLP printed IBU MNs disrupted stratum corneum layer of rat skin where needles dissolved and released the drug in dermal region. Data also showed about 1000 ng/mL IBU in rat plasma at the end of 48 hr which indicated that IBU MN patches developed in this study can be used for sustained delivery of a lipophilic small molecule API over multiple days. Nagai et al. formulated a topical IBU gel system on rats for its systemic absorption and showed an IBU Cmax of approximately 2.3 nmol/ml (475.87 ng/mL) following topical doses of approximately 15 mg which was significantly less compared to our peak results of about 3717.43 $\pm$ 782.25 (ng/ml) following an absorbable dose of around 10 mg (Nagai et al., 2016). This indicates that MNs can significantly enhance the systemic absorption of APIs compared to semisolid formulations by disrupting the stratum corneum barrier of the skin.

The mechanism of patch performance in vivo was investigated using pharmacokinetic modeling of the data, which demonstrated a dual mechanism of input with parallel biphasic first order burst and zero order input for both rapid and sustained absorption from the microneedle patch. The rapid burst phase shown is likely due to the needle cones overcoming any permeability limitation of the stratum corneum, and/or its high dissolvable surface area. Assuming literature PK values for ibuprofen in rats (Vd $\approx$ 0.4L, T1.2 elim $\approx$ 1.8 hrs), the total calculated dose of 10 mg at 48 h provides drug exposure of 63,694 ug*hr/L, (i.e. AUC = Dose/Ke*Vd) which was comparable to the noncompartmental $AUC_{0\text{-}48h}$ calculated in this study (Yang et al., 2015, Gola et al., 2016). Comparing ex vivo permeation and in vivo input was insightful as the steady state flux after 24 h observed from ex vivo skin permeation (25ug/cm2/hr) from a single patch with 2.25 square centimeters (i.e. 1.5 cm $\times$ 1.5 cm) was comparable to the zero order input rate of approximately 160 ug/hr from two patches (i.e., 80ug/hr in vivo versus approximately 56ug/hr ex vivo). A predictive relationship between in vitro dissolution release media and in vivo absorption from the microneedle patch was also explored as we were interested in a potential correlation between microneedles which are beyond the stratum corneum and the direct in vitro release profile. As revealed by the fraction absorbed plot in vivo, we clearly observed a biphasic release mechanism which necessitated fitting a nonlinear in vitro-in vivo relationship (IVIVR). The IVIVC helped us identify whether the in vivo model was rate limited by the physiological system or was more dependent on the dissolvable delivery system. The IVIVR analysis and its nonlinear relationship suggested that there are permeability and/or perfusion limitations during the burst phase (in lieu of dissolution controlled absorption) prior to zero order controlled delivery.

Overall, in the present study, resin formulation compatible with SLA and DLP printing technology has been developed. SLA printer was successfully modified to evaluate the resin printability using significantly low quantity of resin. However, unlike DLP, SLA printing didn't produce desired MN morphology with aspect ratio of 3 and RoC of 15. Therefore, IBU MN patch was optimized using DLP printer by applying QbD and AI approaches. Further, the optimized IBU MNs were able to form pores in the skin as suggested by mechanical strength studies. In vitro data suggests that IBU MNs dissolved in the human dermatomed skin in IVPT study and released drug continuously for 72 h. In vivo PK data showed systemic absorption of drug from MNs when applied on SD rats. IVIVR study was consistent with a biphasic rapid first order parallel zero order release mechanism from IBU MNs.

5. Conclusion

Our results revealed that 3D DLP printed IBU MNs were successfully optimized using AI supplemented with QbD approach. Further, our in vivo studies showed systemic absorption of IBU from the 3D printed MN patch with biphasic first and zero order release.

CRediT authorship contribution statement

Arvind Bagde: Conceptualization, Methodology, Formal analysis, Investigation, Writing – original draft, Visualization, Writing – review & editing. **Satyanarayan Dev:** Conceptualization, Methodology, Formal analysis, Investigation. **Lalitha Madhavi K. Sriram:** Software, Validation, Formal analysis. **Shawn D. Spencer:** Software, Validation, Formal analysis. **Anilkumar Kalvala:** Investigation. **Aakash Nathani:** Investigation. **Oluwaseyi Salau:** Investigation. **Keb Mosley-Kellum:** Investigation. **Harshil Dalvaigari:** Investigation. **Swaminathan Rajaraman:** Investigation. **Avra Kundu:** Investigation. **Mandip Singh:** Writing – review & editing, Resources, Supervision, Project administration, Funding acquisition.

Declaration of Competing Interest

The authors declare that they have no known competing financial interests or personal relationships that could have appeared to influence the work reported in this paper.

Data availability

Data will be made available on request.

Acknowledgments

The research was supported by the National Institute on Minority Health and Health Disparities of National Institutes of Health under Award number U54 MD007582 (U54 RCMI grant) and NSF-CREST Center for Complex Materials Design for Multidimensional Additive Processing (CoManD) award # 1735968.

Appendix A. Supplementary data

Supplementary data to this article can be found online at https://doi.org/10.1016/j.ijpharm.2023.122647.

References

Affram, K., Udofot, O., Singh, M., Krishnan, S., Reams, R., Rosenberg, J., Agyare, E., 2017. Smart thermosensitive liposomes for effective solid tumor therapy and in vivo imaging. PLoS One 12 (9), e0185116.

Aksu, B., Paradkar, A., de Matas, M., Özer, Ö., Güneri, T., York, P., 2012. Quality by design approach: application of artificial intelligence techniques of tablets manufactured by direct compression. AAPS PharmSciTech 13 (4), 1138–1146.

Al-Saidan, S., 2004. Transdermal self-permeation enhancement of ibuprofen. J. Control. Release 100 (2), 199–209.

Altuna, A., Gabriel, G., de la Prida, L.M., Tijero, M., Guimerá, A., Berganzo, J., Salido, R., Villa, R., Fernández, L.J., 2010. SU-8-based microneedles for in vitro neural applications. J. Micromech. Microeng. 20 (6), 064014.

Bagde, A., Patel, K., Kutlehria, S., Chowdhury, N., Singh, M., 2019a. Formulation of topical ibuprofen solid lipid nanoparticle (SLN) gel using hot melt extrusion technique (HME) and determining its anti-inflammatory strength. Drug Deliv. Transl. Res. 9 (4), 816–827.

Bagde, A., Patel, K., Mondal, A., Kutlehria, S., Chowdhury, N., Gebeyehu, A., Patel, N., Kumar, N., Singh, M., 2019b. Combination of UVB absorbing titanium dioxide and quercetin nanogel for skin cancer chemoprevention. AAPS PharmSciTech 20 (6), 1–12.

Care, I. o. L. A. R. C. o. and U. o. L. Animals (1986). Guide for the care and use of laboratory animals, US Department of Health and Human Services, Public Health Service, National ….

Cheung, K., Han, T., Das, D.B., 2014. Effect of force of microneedle insertion on the permeability of insulin in skin. J. Diabetes Sci. Technol. 8 (3), 444–452.

Chowdhury, N., Vhora, I., Patel, K., Doddapaneni, R., Mondal, A., Singh, M., 2017. Liposomes co-loaded with 6-phosphofructo-2-kinase/fructose-2, 6-biphosphatase 3 (PFKFB3) shRNA plasmid and docetaxel for the treatment of non-small cell lung cancer. Pharm. Res. 34 (11), 2371–2384.

Council, N. R. (2010). "Guide for the care and use of laboratory animals.".

Dayal, P., Pillay, V., Babu, R.J., Singh, M., 2005. Box-Behnken experimental design in the development of a nasal drug delivery system of model drug hydroxyurea: characterization of viscosity, in vitro drug release, droplet size, and dynamic surface tension. AAPS PharmSciTech 6 (4), E573–E585.

Duchi, S., Onofrillo, C., O'Connell, C.D., Blanchard, R., Augustine, C., Quigley, A.F., Kapsa, R.M., Pivonka, P., Wallace, G., Di Bella, C., 2017. Handheld co-axial bioprinting: application to in situ surgical cartilage repair. Sci. Rep. 7 (1), 1–12.

Economidou, S.N., Pere, C.P.P., Reid, A., Uddin, M.J., Windmill, J.F., Lamprou, D.A., Douroumis, D., 2019. 3D printed microneedle patches using stereolithography (SLA) for intradermal insulin delivery. Mater. Sci. Eng. C 102, 743–755.

Fairbanks, B.D., Schwartz, M.P., Bowman, C.N., Anseth, K.S., 2009. Photoinitiated polymerization of PEG-diacrylate with lithium phenyl-2, 4, 6-trimethylbenzoyl-phosphinate: polymerization rate and cytocompatibility. Biomaterials 30 (35), 6702–6707.

Fu, Y., Saraswat, A., Wei, Z., Agrawal, M.Y., Dukhande, V.V., Reznik, S.E., Patel, K., 2021. Development of Dual ARV-825 and Nintedanib-Loaded PEGylated Nano-Liposomes for Synergistic Efficacy in Vemurafnib-Resistant Melanoma. Pharmaceutics 13 (7), 1005.

Fulzele, S.V., Babu, R., Ahaghotu, E., Singh, M., 2007. Estimation of proinflammatory biomarkers of skin irritation by dermal microdialysis following exposure with irritant chemicals. Toxicology 237 (1–3), 77–88.

Godugu, C., Doddapaneni, R., Singh, M., 2017. Honokiol nanomicellar formulation produced increased oral bioavailability and anticancer effects in triple negative breast cancer (TNBC). Colloids Surf. B Biointerfaces 153, 208–219.

Gola, S., Gupta, A., Keshri, G.K., Nath, M., Velpandian, T., 2016. Evaluation of hepatic metabolism and pharmacokinetics of ibuprofen in rats under chronic hypobaric hypoxia for targeted therapy at high altitude. J. Pharm. Biomed. Anal. 121, 114–122.

Griffin, T., Rybak, M., Recht, L., Singh, M., Salimi, A., Raso, V., 1993. Potentiation of antitumor immunotoxins by liposomal monensin. JNCI: Journal of the National Cancer Institute 85 (4), 292–298.

Hoffmann, W., Gradinaru, J., Farcal, L., Caul-Futy, M., Huang, S., Wiszniewski, L., Parissis, N., Morath, S., Fortaner, S., Cole, T., 2018. Establishment of a human 3D tissue-based assay for upper respiratory tract absorption. Applied in vitro Toxicology 4 (2), 139–148.

Johnson, A.R., Caudill, C.L., Tumbleston, J.R., Bloomquist, C.J., Moga, K.A., Ermoshkin, A., Shirvanyants, D., Mecham, S.J., Luft, J.C., DeSimone, J.M., 2016. Single-step fabrication of computationally designed microneedles by continuous liquid interface production. PLoS One 11 (9), e0162518.

Kandimalla, K.K., Kanikkannan, N., Singh, M., 1999. Optimization of a vehicle mixture for the transdermal delivery of melatonin using artificial neural networks and response surface method. J. Control. Release 61 (1–2), 71–82.

Khosraviboroujeni, A., Mirdamadian, S.Z., Minaiyan, M., Taheri, A., 2022. Preparation and characterization of 3D printed PLA microneedle arrays for prolonged transdermal drug delivery of estradiol valerate. Drug Deliv. Transl. Res. 12 (5), 1195–1208.

Kulkarni, S.B., Singh, M., Betageri, G.V., 1997. Encapsulation, Stability and In-vitro Release Characteristics of Liposomal Formulations of Colchicine. J. Pharm. Pharmacol. 49 (5), 491–495.

Kundu, A., Arnett, P., Bagde, A., Azim, N., Kouagou, E., Singh, M., Rajaraman, S., 2020. DLP 3D Printed "Intelligent" Microneedle Array (iμNA) for Stimuli Responsive Release of Drugs and Its in Vitro and ex Vivo Characterization. J. Microelectromech. Syst. 29 (5), 685–691.

Kutlehria, S., Dinh, T.C., Bagde, A., Patel, N., Gebeyehu, A., Singh, M., 2020. High-throughput 3D bioprinting of corneal stromal equivalents. J. Biomed. Mater. Res. B Appl. Biomater. 108 (7), 2981–2994.

Larrañeta, E., Moore, J., Vicente-Pérez, E.M., González-Vázquez, P., Lutton, R., Woolfson, A.D., Donnelly, R.F., 2014. A proposed model membrane and test method for microneedle insertion studies. Int. J. Pharm. 472 (1–2), 65–73.

Lim, S.H., Kathuria, H., Amir, M.H.B., Zhang, X., Duong, H.T., Ho, P.-C.-L., Kang, L., 2021. High resolution photopolymer for 3D printing of personalised microneedle for transdermal delivery of anti-wrinkle small peptide. J. Control. Release 329, 907–918.

Lu, Y., Mantha, S.N., Crowder, D.C., Chinchilla, S., Shah, K.N., Yun, Y.H., Wicker, R.B., Choi, J.-W., 2015. Microstereolithography and characterization of poly (propylene fumarate)-based drug-loaded microneedle arrays. Biofabrication 7 (4), 045001.

Lutton, R.E., Moore, J., Larrañeta, E., Ligett, S., Woolfson, A.D., Donnelly, R.F., 2015. Microneedle characterisation: the need for universal acceptance criteria and GMP specifications when moving towards commercialisation. Drug Deliv. Transl. Res. 5 (4), 313–331.

Manzano, J.S., Wang, H., Slowing, I.I., 2019. High throughput screening of 3d printable resins: adjusting the surface and catalytic properties of multifunctional architectures. ACS Applied Polymer Materials 1 (11), 2890–2896.

McCrudden, M.T., Alkilani, A.Z., McCrudden, C.M., McAlister, E., McCarthy, H.O., Woolfson, A.D., Donnelly, R.F., 2014. Design and physicochemical characterisation of novel dissolving polymeric microneedle arrays for transdermal delivery of high dose, low molecular weight drugs. J. Control. Release 180, 71–80.

Migdadi, E.M., Courtenay, A.J., Tekko, I.A., McCrudden, M.T., Kearney, M.-C., McAlister, E., McCarthy, H.O., Donnelly, R.F., 2018. Hydrogel-forming microneedles enhance transdermal delivery of metformin hydrochloride. J. Control. Release 285, 142–151.

Nagai, N., Tanino, T., Ito, Y., 2016. Pharmacokinetic studies of gel system containing ibuprofen solid nanoparticles. J. Oleo Sci. 65 (12), 1045–1053.

Nguyen, H.X., Banga, A.K., 2017. Fabrication, characterization and application of sugar microneedles for transdermal drug delivery. Ther. Deliv. 8 (5), 249–264.

Nguyen, H.X., Bozorg, B.D., Kim, Y., Wieber, A., Birk, G., Lubda, D., Banga, A.K., 2018. Poly (vinyl alcohol) microneedles: fabrication, characterization, and application for transdermal drug delivery of doxorubicin. Eur. J. Pharm. Biopharm. 129, 88–103.

Nguyen, A.K., Goering, P.L., Reipa, V., Narayan, R.J., 2019. Toxicity and photosensitizing assessment of gelatin methacryloyl-based hydrogels photoinitiated with lithium phenyl-2, 4, 6-trimethylbenzoylphosphinate in human primary renal proximal tubule epithelial cells. Biointerphases 14 (2), 021007.

Nukala, P.K., Palekar, S., Patki, M., Patel, K., 2019a. Abuse deterrent immediate release egg-shaped tablet (egglets) using 3D printing technology: quality by design to optimize drug release and extraction. AAPS PharmSciTech 20 (2), 1–12.

Nukala, P.K., Palekar, S., Solanki, N., Fu, Y., Patki, M., Shohatee, A.A., Trombetta, L., Patel, K., 2019b. Investigating the application of FDM 3D printing pattern in preparation of patient-tailored dosage forms. J. 3D Print. Med. 3 (1), 23–37.

Palekar, S., Nukala, P.K., Mishra, S.M., Kipping, T., Patel, K., 2019. Application of 3D printing technology and quality by design approach for development of age-appropriate pediatric formulation of baclofen. Int. J. Pharm. 556, 106–116.

Palekar, S., Nukala, P.K., Patel, K., 2022. Aversion liquid-filled drug releasing capsule (3D-RECAL): A novel technology for the development of immediate release abuse deterrent formulations using a fused deposition modelling (FDM) 3D printer. Int. J. Pharm. 621, 121804.

Patel, G., Chougule, M., Singh, M., Misra, A., 2009. Nanoliposomal dry powder formulations. Methods Enzymol. 464, 167–191.

Patel, A.R., Chougule, M., Singh, M., 2014. EphA2 targeting pegylated nanocarrier drug delivery system for treatment of lung cancer. Pharm. Res. 31 (10), 2796–2809.

Patel, K., Doddapaneni, R., Chowdhury, N., Boakye, C.H., Behl, G., Singh, M., 2016a. Tumor stromal disrupting agent enhances the anticancer efficacy of docetaxel loaded PEGylated liposomes in lung cancer. Nanomedicine 11 (11), 1377–1392.

Patel, K., Doddapaneni, R., Sekar, V., Chowdhury, N., Singh, M., 2016b. Combination approach of YSA peptide anchored docetaxel stealth liposomes with oral antifibrotic agent for the treatment of lung cancer. Mol. Pharm. 13 (6), 2049–2058.

Pere, C.P.P., Economidou, S.N., Lall, G., Ziraud, C., Boateng, J.S., Alexander, B.D., Lamprou, D.A., Douroumis, D., 2018. 3D printed microneedles for insulin skin delivery. Int. J. Pharm. 544 (2), 425–432.

Shaik, M.S., Ikediobi, O., Turnage, V.D., McSween, J., Kanikkannan, N., Singh, M., 2001. Long-circulating monensin nanoparticles for the potentiation of immunotoxin and anticancer drugs. J. Pharm. Pharmacol. 53 (5), 617–627.

Shaik, M.S., Chatterjee, A., Singh, M., 2004. Effects of monensin liposomes on the cytotoxicity, apoptosis and expression of multidrug resistance genes in doxorubicin-resistant human breast tumour (MCF-7/dox) cell-line. J. Pharm. Pharmacol. 56 (7), 899–907.

Singh, M., Ferdous, A.J., Jackson, T.L., 1999. Stealth monensin liposomes as a potentiator of adriamycin in cancer treatment. J. Control. Release 59 (1), 43–53.
Sriram, L.M.K., Gilanifar, M., Zhou, Y., Ozguven, E.E., Arghandeh, R., 2018. Causal Markov Elman network for load forecasting in multinetwork systems. IEEE Trans. Ind. Electron. 66 (2), 1434–1442.
Sriram, L.M.K., Ulak, M.B., Ozguven, E.E., Arghandeh, R., 2019. Multi-network vulnerability causal model for infrastructure co-resilience. IEEE Access 7, 35344–35358.
Stavrinidis, G., Michelakis, K., Kontomitrou, V., Giannakakis, G., Sevrisarianos, M., Sevrisarianos, G., Chaniotakis, N., Alifragis, Y., Konstantinidis, G., 2016. SU-8 microneedles based dry electrodes for Electroencephalogram. Microelectron. Eng. 159, 114–120.
Than, A., Liu, C., Chang, H., Duong, P.K., Cheung, C.M.G., Xu, C., Wang, X., Chen, P., 2018. Self-implantable double-layered micro-drug-reservoirs for efficient and controlled ocular drug delivery. Nat. Commun. 9 (1), 1–12.
Uddin, M.J., Scoutaris, N., Economidou, S.N., Giraud, C., Chowdhry, B.Z., Donnelly, R.F., Douroumis, D., 2020. 3D printed microneedles for anticancer therapy of skin tumours. Mater. Sci. Eng. C 107, 110248.
Wagner, J.G., Nelson, E., 1964. Kinetic analysis of blood levels and urinary excretion in the absorptive phase after single doses of drug. J. Pharm. Sci. 53 (11), 1392–1403.
Welling, P.G., 1983. Oral controlled drug administration, Pharmacokinetic Considerations. Drug Dev. Ind. Pharm. 9 (7), 1185–1225.
Xenikakis, I., Tzimtzimis, M., Tsongas, K., Andreadis, D., Demiri, E., Tzetzis, D., Fatouros, D.G., 2019. Fabrication and finite element analysis of stereolithographic 3D printed microneedles for transdermal delivery of model dyes across human skin in vitro. Eur. J. Pharm. Sci. 137, 104976.
Yang, Y., Manda, P., Pavurala, N., Khan, M.A., Krishnaiah, Y.S., 2015. Development and validation of in vitro–in vivo correlation (IVIVC) for estradiol transdermal drug delivery systems. J. Control. Release 210, 58–66.
Yang, Q., Zhong, W., Xu, L., Li, H., Yan, Q., She, Y., Yang, G., 2021. Recent progress of 3D-printed microneedles for transdermal drug delivery. Int. J. Pharm. 593, 120106.
Yao, W., Li, D., Zhao, Y., Zhan, Z., Jin, G., Liang, H., Yang, R., 2019. 3D printed multi-functional hydrogel microneedles based on high-precision digital light processing. Micromachines 11 (1), 17.
Zhang, Y., Huo, M., Zhou, J., Xie, S., 2010. PKSolver: An add-in program for pharmacokinetic and pharmacodynamic data analysis in Microsoft Excel. Comput. Methods Prog. Biomed. 99 (3), 306–314.